Suspended Nanoscale Field Emitter Devices for High-Temperature Operation

Lucia B. De Rose, Axel Scherer, and William M. Jones

***Abstract*— In this work, we demonstrate suspended two- and four-terminal field emission devices for high-temperature operation. The planar structures were fabricated with tungsten on a 200-nm silicon nitride membrane. The insulator in the vicinity of the terminals was removed to minimize undesirable Frenkel–Poole emission and increase the resistance of leakage current pathways. The effects of temperatures up to 450 °C on Fowler–Nordheim emission characteristics and parasitic leakage resistance were studied. Turn-on voltages with magnitudes under 15 V that further decreased as a function of increasing temperature for the two-terminal device were reported. Gating at temperatures of 150 °C and 300 °C was shown for the four-terminal device, and corresponding transconductance and cutoff frequency values were computed.**

***Index Terms*— Electron emission, Fowler–Nordheim field emission, Frenkel–Poole emission, high-temperature, leakage current, metallic emitter, vacuum microelectronics.**

I. Introduction

VACUUM field emission devices have been investigated for decades [1], [2] for various applications, including as sources in electron beam lithography [3], flat panel displays [4], microwave power amplifiers [5], and space propulsion systems [6]. Since electrons in vacuum can travel faster and with less energy dissipation than in semiconductors due to the absence of electron–phonon scattering [7], field emission devices can operate at higher frequencies [8] and higher power [9]. Moreover, it is often claimed that field emission devices are more robust and could operate in higher temperature environments [10], [11] than their solid-state counterparts. As temperature increases, semiconductor device operation is limited by the increase of the intrinsic carrier population [12]. This eliminates the effectiveness of chemical doping in controlling the carrier population. In this way, the semiconductor industry has moved toward wide bandgap semiconductors, such as silicon carbide (SiC) and gallium nitride (GaN) [13]. Metal field emitters, on the other hand, do not rely on chemical doping for their device operation. Thus, they are relatively insensitive to temperature changes until the onset of thermionic emission. High-temperature electronics are indispensable for many industries, including aerospace, defense, automotive, and deep oil and gas extraction [14]. In addition, since elevated temperatures promote the desorption of surface contaminants, field emission devices should have more stable electrical performance in these environments than at room temperature [15].

However, several practical nanoscale vacuum devices have insulators near where emission takes place [16]–[18]. The combination of the large electric field required for field emission with a high-temperature environment in an insulator can be detrimental to device operation as it leads to undesirable Frenkel–Poole current leakage [19], [20]. This is the field-assisted thermal ionization effect by which an insulator becomes electrically conductive before reaching dielectric breakdown [21], [22]. One approach to reduce the effect of this parasitic leakage pathway that competes with the Fowler–Nordheim field emission is to distance the insulator from the emission area [23]. In this article, we will show the fabrication and testing at various temperatures of in-plane metallic vacuum field emitters suspended on a silicon nitride membrane. The insulator in the vicinity of the high electric field region will be removed to prevent Frenkel–Poole emission. We will use tungsten, a refractory metal, as our electrode material due to its low work function (approximately 4.5 eV [24]) as well as its high-temperature tolerance.

II. Fabrication

The devices were fabricated on a suspended, stoichiometric silicon nitride (Si_3N_4) membrane with planar dimensions of 5 mm × 5 mm and a thickness of 200 nm (Norcada QX10500DS). The suspended membrane was laterally supported by a 200-μm-thick silicon frame. Standard electron beam lithography was used to pattern connected terminals, interconnect lines, alignment marks, and contact pads. The contact pads were written on the supporting silicon frame. A conducting layer consisting of 150 nm of tungsten with a 7-nm titanium adhesion layer was sputtered in an ultrahigh vacuum magnetron sputtering system (AJA). Subsequent lift-off was performed in acetone. Aligned electron beam lithography was used to redefine the electrical contact pads, onto

Manuscript received June 26, 2020; revised August 20, 2020; accepted August 24, 2020. Date of publication September 9, 2020; date of current version October 22, 2020. This work was supported in part by the NASA/ROSES HOTTECH Program 80HQTR17C0011 under a subcontract from the Boeing Company and in part by the President and Director's Fund at the California Institute of Technology and the Jet Propulsion Laboratory under Award 1614028. The review of this article was arranged by Editor M. Blank. *(Corresponding author: Lucia B. De Rose.)*

Lucia B. De Rose and Axel Scherer are with the Department of Applied Physics, California Institute of Technology, Pasadena, CA 91125 USA (e-mail: lderose@caltech.edu).

William M. Jones is with the Jet Propulsion Laboratory, California Institute of Technology, Pasadena, CA 91109 USA.

Color versions of one or more of the figures in this article are available online at http://ieeexplore.ieee.org.

Digital Object Identifier 10.1109/TED.2020.3019765

This work is licensed under a Creative Commons Attribution 4.0 License. For more information, see https://creativecommons.org/licenses/by/4.0/

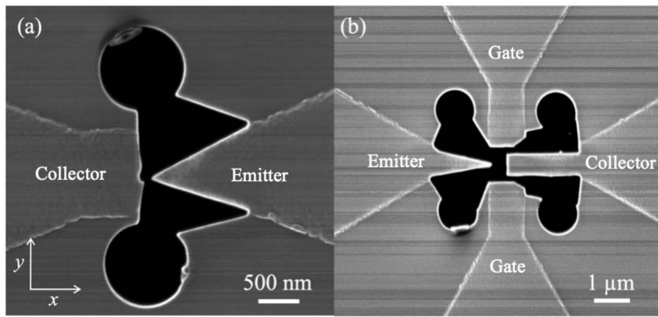

Fig. 1. (a) Ion micrograph of suspended two-terminal diode-like device and (b) four-terminal triode-like device. In (a), the emitter–collector gap is measured to be 95 nm, and in (b), the emitter–collector gap is measured to be 367 nm.

which a layer consisting of 150-nm gold with a titanium adhesion layer was deposited. The thicker contact layer allows ultrasonic wirebonding to connect the devices without punching through the silicon nitride layer to the partially conductive silicon frame.

The connected terminals were manually separated by means of neon focused ion beam (FIB) patterning (Zeiss Orion NanoFab). This allowed the creation of both two-terminal diode-like [see Fig. 1(a)] and four-terminal triode-like lateral devices [see Fig. 1(b)]. In both cases, one of the terminals, the so-called "emitter," was sharpened so that it has a larger field-enhancement factor compared with the other terminals and, thus, emits at a smaller applied bias. This step yielded a macroscopic tip diameter of approximately 10 nm in Fig. 1(a) and around 40 nm in Fig. 1(b). In the two-terminal device, our intention is that this asymmetric geometry created by the sharp emitter and the blunt collector will allow us to mimic current–voltage (I–V) curves' characteristic to diodes. In the four-terminal device, we focus on maximizing the field enhancement of a single terminal to minimize the leakage of field-emitted currents from either the on-axis collector or the off-axis gates.

Before ion milling, the membrane was coated with a thin conductive carbon layer for charge dissipation. In order to prevent crack propagation and relieve stress, two stop holes on the off-axis plane of the terminals were milled before the terminals were separated. This removed the possibility of sharp corners that could serve as nucleation sites for cracks in the silicon nitride [25]. The FIB patterning was also used to remove the silicon nitride membrane in the vicinity of the terminals, thus minimizing a potential leakage pathway across the insulating substrate. Finally, the membrane was subjected to oxygen plasma etching to remove the conductive carbon layer.

III. Results and Discussion

The membrane was ultrasonically wedge wire-bonded with aluminum wires to conductive strips on a 1-in^2 ceramic substrate. The membrane and the substrate were placed on top of a vacuum-safe heater (HeatWave Labs) with a thermocouple attached to the surface of the ceramic substrate inside of a stainless-steel vacuum system. The membrane, ceramic substrate, and thermocouple were held via compression by temperature-resistant molybdenum springs. A photograph of

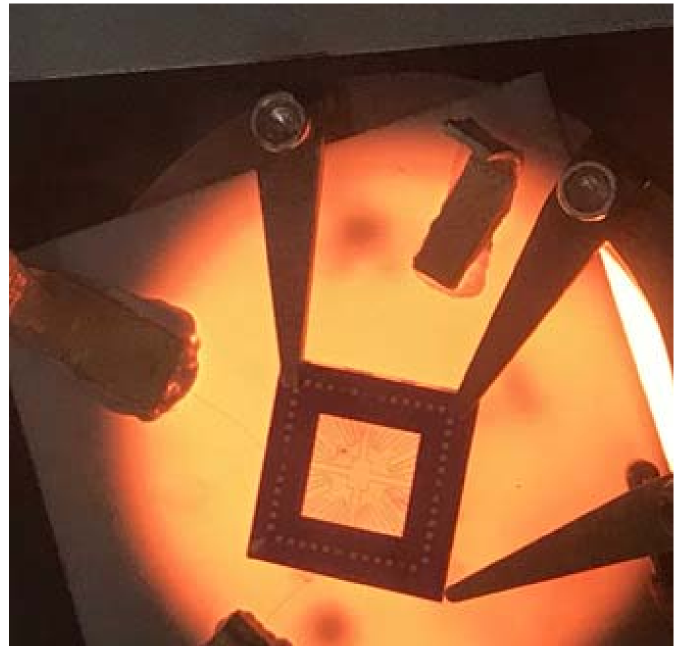

Fig. 2. Photograph of wire-bonded membrane and ceramic substrate sitting on top of heater.

this setup is shown in Fig. 2. The strips on the ceramic substrate were connected to the electrical feedthrough of a vacuum chamber that routed to automated electrical picoammeters/voltage sources (Keithley 6487). Each terminal was linked to a separate picoammeter so that the bias of each terminal could be independently controlled, and the current at each terminal could be measured. In addition, 10-MΩ current-limiting resistors were placed in series with each of the terminals as ballast resistors to prevent both thermal runaway and surge currents. The vacuum chamber was pumped to $\sim 10^{-7}$ Torr and baked for several hours with the sample temperature held at 150 °C before testing to assist with the desorption of water vapor and other contaminants from the surface of the various terminals. After all tests were completed on the membrane, the devices showed no visible changes in morphology when inspected via scanning electron micrography.

Multiple I–V scans per device with a forward and reverse sweep were first taken at 150 °C in order to remove further adsorbates from the emitting surfaces. This "conditioning" [26] process was repeated until the turn-on voltage appeared to be stable. Turn-on voltage was defined as the voltage that yields a current above the noise floor (approximately 5 nA). We selected this threshold current value to be 15 nA. Fig. 3(a) shows the I–V plot for the diode-like device shown in Fig. 1(a) tested from 150 °C up to 450 °C in increments of 50 °C. The emitter to collector gap was measured to be 95 nm. The emitter voltage V is defined as $V = V_A - IR$, where V_A is the applied voltage on the emitter, I is the emission current, and R is the series resistance of the ballast resistors. A current limit of 100 nA is imposed to prevent excessive resistive heating and potential tip destruction. The emission current from a metallic surface can be expressed by the so-called elementary Fowler–Nordheim equation

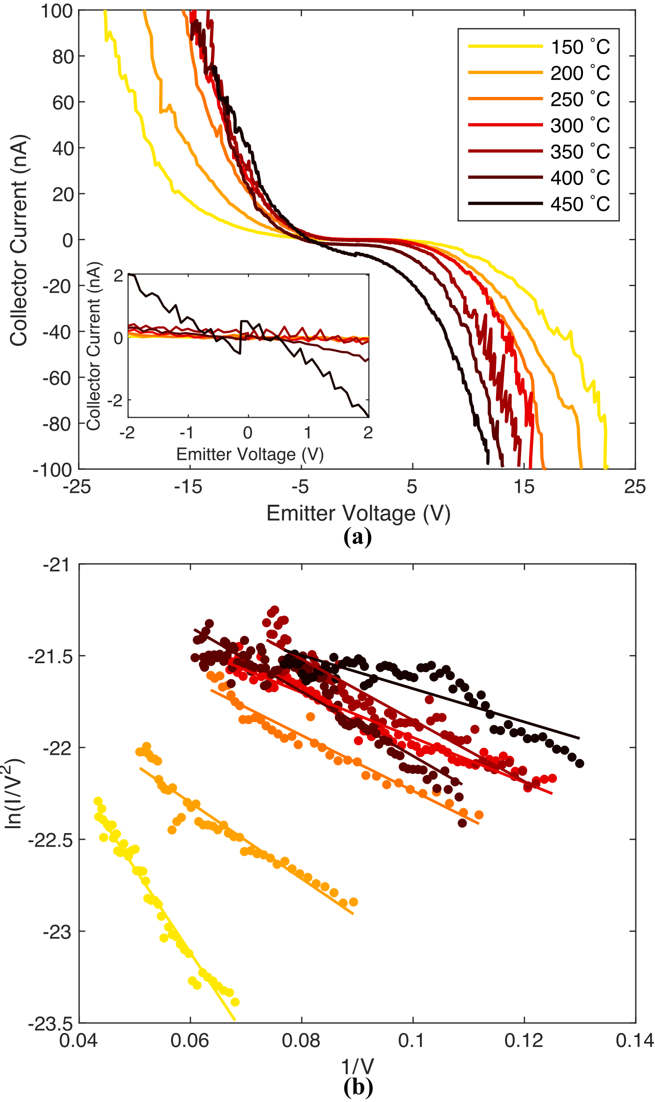

Fig. 3. (a) I–V characteristic for the two-terminal device removing the series resistance and (b) its Fowler–Nordheim plot for currents over 15 nA for temperatures between 150 °C and 450 °C. The lines correspond to the least-squares regression.

given by [27], [28]

$$I = \frac{Aa_{FN}}{\varphi}E^2 \exp\left(-\frac{b_{FN}\varphi^{3/2}}{E}\right) \tag{1}$$

with

$$a_{FN} = \frac{e^3}{16\pi^2\hbar} \approx 1.54\ \mu\text{A} \cdot \text{eV} \cdot \text{V}^{-2}$$

and

$$b_{FN} = \frac{4}{3e}\left(\frac{2m}{\hbar^2}\right)^{1/2} \approx 6.83\ \text{V} \cdot \text{nm}^{-1} \cdot \text{eV}^{-3/2}$$

where A is the effective emission area, φ is the local work function, E is the local electric field at the tip, and e and m are the elementary charge and mass of the electron, respectively. In addition, E is related to the applied voltage by $E = \beta V$, where β is the field factor. We can also relate the local electric field E to the distance between the emitter and collector d by the relation $E = \gamma(V/d)$, where γ is a dimensionless

TABLE I

TWO-TERMINAL DEVICE DATA AS A FUNCTION OF TEMPERATURE

Temperature (°C)	Parallel Leakage Resistance (GΩ)	Slope	y-intercept	R^2 value
150	94.0	-45.95	-20.36	0.970
200	45.2	-20.73	-21.05	0.916
250	17.6	-15.12	-20.72	0.948
300	7.6	-12.22	-20.72	0.946
350	8.9	-16.64	-20.18	0.909
400	5.4	-17.52	-20.29	0.886
450	0.8	-9.05	-20.77	0.753

parameter called the field-enhancement factor. Since γ is geometry-dependent, a way to maximize it is to sharpen the emitter tip by reducing its radius of curvature [29].

The device displays turn-on voltages with a magnitude of under 13 V. Low turn-on voltages are desirable since they open the possibility for atmospheric pressure operation [30]. As the energy of the electrons is not high enough to ionize the atoms present in the atmosphere, ion bombardment of the terminals can be diminished. Further reductions in the turn-on voltage could be achieved by decreasing the size of the emitter to collector gap [31].

Unfortunately, the emission from either terminal is symmetric. This could be explained by the fact that the collector terminal is not completely blunt but rather has an undesired sharp protrusion, which effectively yields a γ comparable to the one at the emitter tip.

The inset of Fig. 3(a) shows a magnified view of the zero-corrected I–V curve for voltages near 0 V. We can observe that before the onset of field emission, current increases linearly with increasing voltage. This illustrates that parasitic leakage dominates at these small fields. We performed a linear fit of the small field data and extracted the values for the parasitic series resistance at the various temperatures, which are presented in Table I. This parasitic resistance decreases with increasing temperature. Since we have removed the substrate in the vicinity of the high fields, the likely leakage pathway is via the supporting silicon ring, which has a resistivity of 1–30 $\Omega \cdot$cm at room temperature as quoted by the manufacturer.

Fig. 3(b) shows the I–V characteristic in Fowler–Nordheim coordinates for currents above 15 nA to focus on field emission current exclusively. The Fowler–Nordheim coordinates correspond to a linearization transformation applied to (1) given by

$$\ln\left(\frac{I}{V^2}\right) = -\left(\frac{b_{FN}\varphi^{3/2}d}{\gamma}\right)\frac{1}{V} + \ln\left(\frac{Aa_{FN}\gamma^2}{\varphi d^2}\right). \tag{2}$$

The experimental data for temperatures up to 300 °C display linear behavior, in agreement with the Fowler–Nordheim emission mechanism. For temperatures above 350 °C, the fit deteriorates, and the measured current does not seem to follow a purely Fowler–Nordheim behavior. We confirm that the emission current is not thermionic by plotting the emission current in Richardson–Dushman coordinates ($\ln(I/T^2)$ versus $1/T$) [32] for various applied voltages on the emitter, as shown in Fig. 4. Since the resulting plot is clearly nonlinear in nature for all potentials shown, we rule out thermionic emission. Hence, this could suggest thermally promoted field emission.

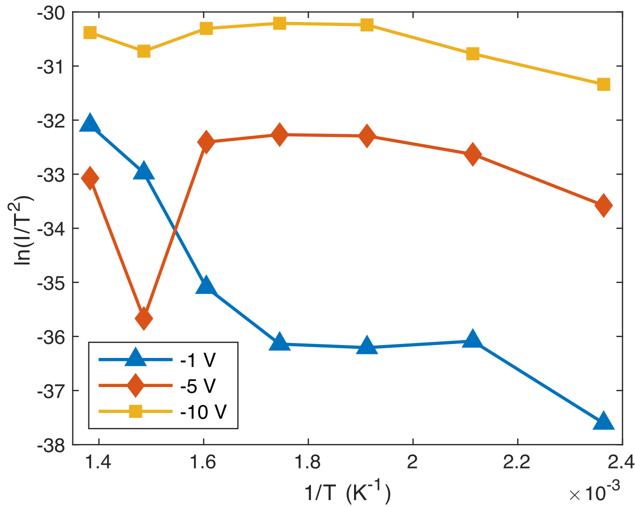

Fig. 4. Emission current in Richardson–Dushman coordinates for various applied voltages.

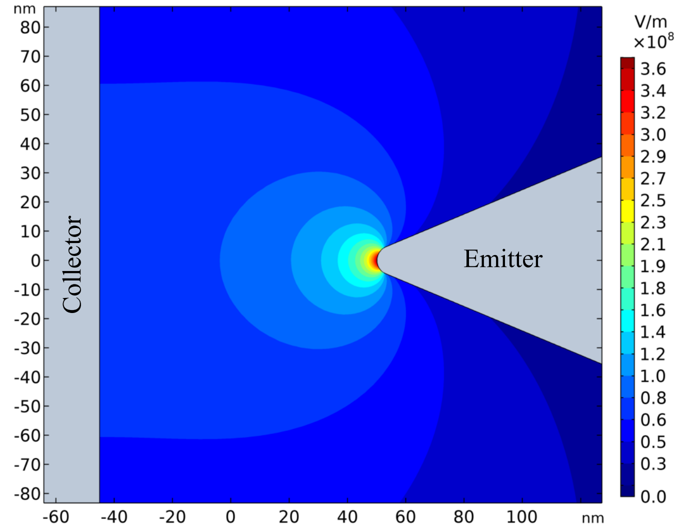

Fig. 5. COMSOL simulation for the diode-like device of the component of the electric field normal to the emitting surface in V/m at −10 V applied on the emitter terminal.

At higher temperatures, thermally excited electrons transmit through a thinner potential barrier as these electrons have the tail of the energy distribution above the Fermi energy. This contribution of thermal electrons and resultant deviation from merely Fowler–Nordheim emission is particularly noticeable for low currents [33], as with higher fields Fowler–Nordheim emission dominates [34]. In addition, this enhanced tunneling probability may also explain the lower turn-on voltages observed at higher temperatures, as, for the same potential, the emission current is larger [35], [36].

Table I shows the values for the slope and y-intercept of the least-squares regression line, along with the value for the coefficient of determination for all measured temperatures. Based on the reported literature work function of tungsten ($\varphi = 4.5$ eV) and the slope of the Fowler–Nordheim plot, a value of 133 for the field-enhancement factor γ is calculated at 150 °C. We perform a 2-D finite element method (FEM) simulation (COMSOL Multiphysics 5.4) based on the device dimension values extracted from the ion micrograph to numerically compute the normal component of the electric field at the emission tip, as illustrated in Fig. 5. The simulation suggests a more modest γ of 3.5, a value two orders of magnitude smaller than what we obtain experimentally. This discrepancy may be due to uncertainty in the efficient emitter tip radius, as emission may be taking place locally at nanoprotusions, grain boundaries, or groups of atoms [37], which may not be accurately resolved via an ion micrograph.

Overall, the magnitude of the slope is decreasing as a function of temperature. As the slope depends on both γ and φ, it could be the case that with increasing temperature, either γ is increasing, φ is decreasing, or a combination of both. An increasing γ could be a consequence of temperature-dependent desorption of residual molecules that alter the surface roughness of the emitter tip [38]. Temperature-induced release of gaseous adsorbates may also explain the potential decrease in φ [39], [40]. Electronegative adsorbates in the emitter surface, such as oxygen, have been shown to increase the work function. In this way, traditional techniques to analyze Fowler–Nordheim plots are challenging to apply [41], as it is hard to remove all contaminants and produce an atomically clean surface.

Next, building upon our two-terminal device, we also fabricate in-plane four-terminal triode-like structures, as shown in Fig. 1(b). The emitter to collector distance is 367 nm. The two structures located off-axis will act as the gates by modulating the electric field at the tip of the emitter, which affects the tunneling probability [42]. Ideally, the y-component of the electric field between the gates and the emitter cancels out, which minimizes the leakage of field-emitted current into the gates. Yet, asymmetries inevitably arise during the fabrication process. In our case, the top gate is 442 nm away from the emitter tip, while the bottom gate is separated by 462 nm. In order to account for this unevenness, the gates are electrically separated, and their bias can be independently controlled.

Fig. 6 shows the I–V curve of the triode-like device for various gate biases tested at 150 °C [see Fig. 6(a)] and 300 °C [see Fig. 6(b)]. The current shown is the emitter current. In this way, we concentrate on Fowler–Nordheim currents between emitter and collector and ignore leakage of field-emitted currents to the gates that will be later addressed. For Fig. 6(a) and (b), the collector is kept at ground. Various combinations for gate bias were tested to minimize the preferential current leakage to an individual gate and achieve as close to a symmetric behavior as possible. Ultimately, this condition was achieved when the bias offset between them was set to +10 V for Fig. 6(a) and +50 V for Fig. 6(b), such that the top gate was at a more negative potential compared with the bottom gate. The gate voltage reported in the plot corresponds to the top gate bias. The runs were not performed in a decreasing gate bias sequence as the legend suggests but in a randomized sequence. This was done to rule out heating effects of the emitter tip as the justification for any observed gating. The device displays turn-on voltages of around −120 V for Fig. 6(a) and −80 V for Fig. 6(b). Once again, we observe thermally promoted field emission, as the

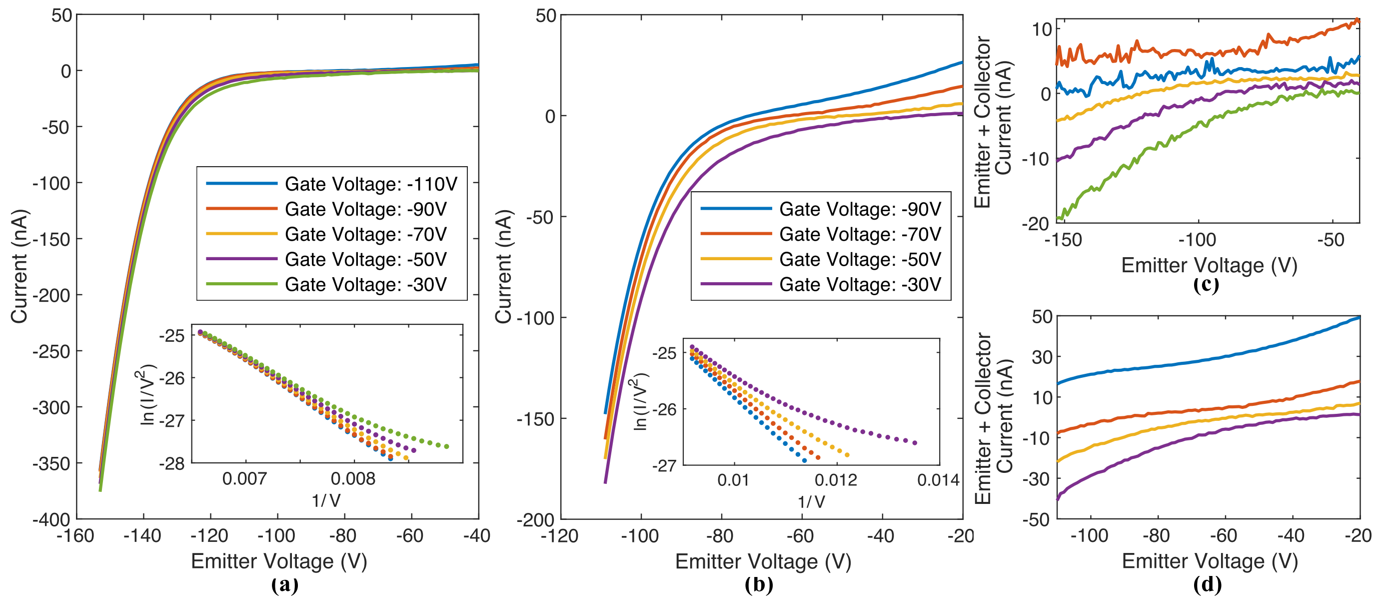

Fig. 6. *I–V* characteristic for triode-like device at various gate bias for (a) 150 °C and (b) 300 °C, respectively. The insets present the data in Fowler–Nordheim coordinates for currents over 15 nA. Added emitter and collector currents to illustrate leakage to the gate terminal for (c) 150 °C and (d) 300 °C.

turn-on voltage becomes smaller at higher temperatures. Yet, these devices display larger turn-on voltages compared with the two-terminal devices previously discussed. This results from the considerably larger emitter-to-collector distance. The insets correspond to the data plotted in Fowler–Nordheim coordinates. The linearity of the plots for higher emitter voltages confirms Fowler–Nordheim current as the emission mechanism. It can be seen that as the gate bias becomes more negative, the measured current is reduced for a given emitter potential. This illustrates the effect of gating at the emitter tip—as the potential difference between emitter and gates decreases, the magnitude of the electric field at the emission tip is reduced, and thus, the emitted current is diminished.

Fig. 6(c) and (d) portrays the addition of the emitter and collector currents (with signs) as a function of emitter bias for the various gate biases for 150 °C and 300 °C, respectively. The purpose of these graphs is to show the field-emitted current leakage from either the emitter to the top gate or from the top gate to the collector. We can ignore the leakage to the bottom gate, as it was measured for all emitter voltages to be consistently under 1 nA for 150 °C and under 7 nA for 300 °C (this value was measured when the leakage to the top gate was the largest). The smaller leakage for the bottom gate may be a consequence of the larger distance to the emitter tip. A positive value in the plots corresponds to collector leakage, while a negative value corresponds to emitter leakage. When the potential difference between the emitter and the gates is increased, current leaks from emitter to gate. The leakage path then changes, with most leakage taking place from gate to collector when the potential difference between the emitter and gates is decreased. Since all currents are monitored, we ensure that no current is unaccounted for. To reduce the emitter to gate leakage, we should improve the symmetry of the gates so that no gate wants to preferentially take any current. To avoid gate to collector leakage, a potential solution could be to fabricate

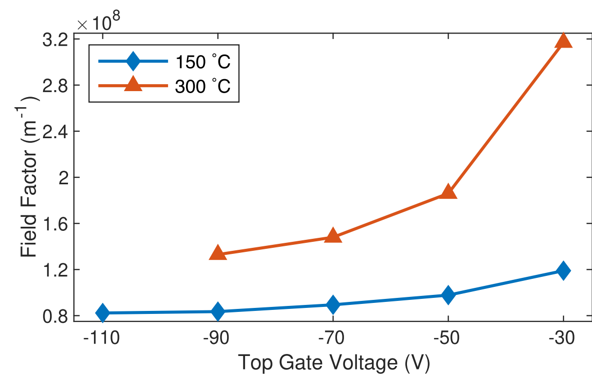

Fig. 7. Calculated field factor for the four-terminal device as a function of top gate voltage for 150 °C and 300 °C.

the gates with a metal of a higher work function and, thereby, hinder the onset of exponential emission.

We fit a linear regression model to the data, and we extract the vertical axis intercept and slope. We consider $\varphi = 4.5$ eV, and we calculate β, as shown in Fig. 7. For both temperatures, β is larger when the potential difference between the emitter and the gates is increased. This agrees with the increase in current for a given emitter voltage when the gate voltage becomes more positive, which confirms that the gate electric field modulates the emission current.

Next, we compare our measured data to a simulation of our device operation. For the simulation, we select the lower temperature data with the smallest average leakage current to the gates (top gate at -70 V), and we calculate an emission area A equal to 6.5 nm^2. We use COMSOL to determine that an emitter tip radius of 0.25 nm is necessary to achieve the β previously calculated (see Fig. 7) for the specific potential configuration. Next, we simulate the expected gating, as shown in Fig. 8(a) and (b). We calculate the expected transconductance g_m from the simulation at -153 V to be 24.5 nS. From the data

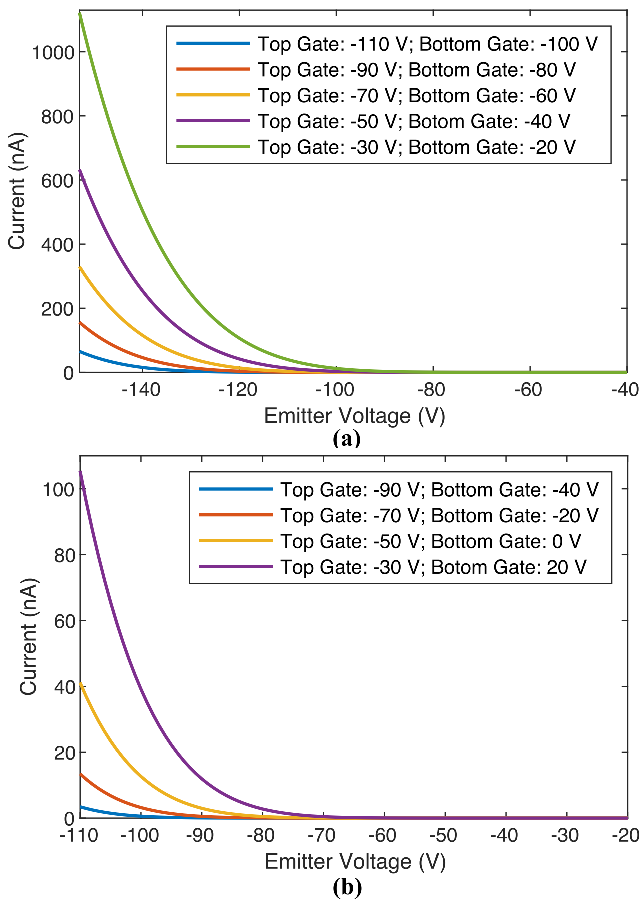

Fig. 8. Simulated *I–V* characteristic for the current device geometry for the various gate potential configurations experimentally tested at (a) 150 °C and (b) 300 °C.

in Fig. 6(a), we calculate an experimental transconductance of 0.3 nS at the same emitter potential. If we use the collector current, this value becomes 0.1 nS. Similarly, we simulate g_m to be 4.9 nS at the maximum emitter voltage tested of -110 V, while the experimental at 300 °C for the same potential is 0.7 nS (and 0.6 nS if we consider collector current). A potential reason to explain the difference between the simulated and the experimentally obtained values is that the simulated transconductance does not consider any leakage to/from the gate, while the experimental data does include this leakage. We then simulate Maxwell's capacitance C for the device to be 7.059×10^{-17} F, and we calculate the experimental cutoff frequency f_c given by $f_c = g_m(2\pi C)^{-1}$ [43] to be 0.676 MHz for 150 °C and 1.578 MHz for 300 °C. Using the simulated g_m, f_c for this geometry could be as high as 55.23 and 11.05 MHz, respectively. This g_m is much less than previously reported values for single-tip field emission transistors. For example, Han *et al.* [17] have demonstrated a gate-insulated vacuum channel transistor with $g_m = 0.2$ μS. In order to increase f_c, we need to increase the transconductance. As the distance between the gates and the emitter affects the field between them, we need to reduce this distance to increase the control of the emitted current. For instance, if we move the gates away from the collector and closer to the emitter such that the distance between the gates and the emitter is 100 nm, the simulated transconductance becomes 130 nS. However, this will unfortunately also increase the capacitance to 8.456×10^{-17} F. In addition, since Fowler–Nordheim current increases exponentially, a larger emitter bias can also increase g_m. Finally, g_m has been found to exponentially increase with the gate potential [44], but this may come at the cost of a higher leakage.

IV. Conclusion

In this work, we have presented suspended lateral two-terminal diode-like and four-terminal triode-like vacuum field emitters. We used tungsten as the material for the emitters due to its low work function and high-temperature tolerance. The two-terminal device was tested for temperatures ranging from 150 °C up to 450 °C and displays turn-on voltages with magnitudes under 15 V. This value further decreased with increasing temperature. A similar effect was shown for the four-terminal device. In addition, the effect of gating was studied, and the values for the transconductance and cutoff frequency were calculated. By shrinking the distance between the emitter and the gates, these values could be further increased by over an order of magnitude while maintaining high-temperature operation.

Acknowledgment

The authors gratefully acknowledge many technical discussions and guidance from Dr. Leora Peltz and Robert Frampton from The Boeing Company. This research was carried out in part at the Jet Propulsion Laboratory, California Institute of Technology, under a contract with the National Aeronautics and Space Administration.

References

[1] R. G. Forbes, J. H. B. Deane, N. Hamid, and H. S. Sim, "Extraction of emission area from Fowler–Nordheim plots," *J. Vac. Sci. Technol. B*, vol. 22, no. 3, p. 1222, 2004, doi: 10.1116/1.1691410.

[2] I. U. Smirnov, A. G. Kolosko, S. V. Filippov, N. A. Yudkina, and E. O. Popov, "Application of slope-intercept diagram to determine the parameters of the nanocomposite field emitters *in-situ*," *J. Phys., Conf. Ser.*, vol. 741, Aug. 2016, Art. no. 012031, doi: 10.1088/1742-6596/741/1/012031.

[3] I. S. Turmyshev, A. M. Murzakaev, and O. R. Timoshenkova, "Field emission from metal tips covered by ultra-thin films of Zirkonia energy spectra features and current-voltage curves," in *Proc. 25th Int. Symp. Discharges Elect. Insul. Vac. (ISDEIV)*, Sep. 2012, pp. 595–598, doi: 10.1109/DEIV.2012.6412590.

[4] W. B. Choi *et al.*, "Fully sealed, high-brightness carbon-nanotube field-emission display," *Appl. Phys. Lett.*, vol. 75, no. 20, pp. 3129–3131, Nov. 1999.

[5] C. A. Spindt, C. M. Armstrong, C. R. Smith, B. M. Gannon, and D. R. Whaley, "Application of field emitter arrays to microwave power amplifiers," *IEEE Trans. Plasma Sci.*, vol. 28, no. 3, pp. 727–747, Jun. 2000.

[6] M. Tajmar, A. Genovese, and W. Steiger, "Indium field emission electric propulsion microthruster experimental characterization," *J. Propuls. Power*, vol. 20, no. 2, pp. 211–218, Mar. 2004.

[7] G. P. Kochanski, W. Zhu, and Y. Goren, "Technological overview," in *Vacuum Microelectronics*. Hoboken, NJ, USA: Wiley, 2001, pp. 13–32.

[8] A. Evtukh, H. Hartnagel, O. Yilmazoglu, H. Mimura, and D. Pavlidis, "Quantum electron sources for high frequency applications," in *Vacuum Nanoelectronic Devices*. Hoboken, NJ, USA: Wiley, 2015, pp. 375–446.

[9] M. Garven, S. N. Spark, A. W. Cross, S. J. Cooke, and A. D. R. Phelps, "Gyrotron experiments employing a field emission array cathode," *Phys. Rev. Lett.*, vol. 77, no. 11, pp. 2320–2323, Sep. 1996.

[10] L. Wang, G. Wei, F. Gao, C. Li, and W. Yang, "High-temperature stable field emission of B-doped SiC nanoneedle arrays," *Nanoscale*, vol. 7, no. 17, pp. 7585–7592, 2015.

[11] W. M. Jones *et al.*, "Field emitters using inverse opal structures," *Adv. Funct. Mater.*, vol. 29, no. 16, Apr. 2019, Art. no. 1808571.

[12] S. M. Sze and K. K. Ng, "Physics and properties of semiconductors—A review," in *Physics of Semiconductor Devices*. Hoboken, NJ, USA: Wiley, 2006, pp. 5–75.

[13] P. G. Neudeck, R. S. Okojie, and L.-Y. Chen, "High-temperature electronics—A role for wide bandgap semiconductors?" *Proc. IEEE*, vol. 90, no. 6, pp. 1065–1076, Jun. 2002.

[14] X. Guo, Q. Xun, Z. Li, and S. Du, "Silicon carbide converters and MEMS devices for high-temperature power electronics: A critical review," *Micromachines*, vol. 10, no. 6, p. 406, Jun. 2019.

[15] W. P. Dyke, F. M. Charbonnier, R. W. Strayer, R. L. Floyd, J. P. Barbour, and J. K. Trolan, "Electrical stability and life of the heated field emission cathode," *J. Appl. Phys.*, vol. 31, no. 5, pp. 790–805, May 1960.

[16] A. Di Bartolomeo *et al.*, "Leakage and field emission in side-gate graphene field effect transistors," *Appl. Phys. Lett.*, vol. 109, no. 2, Jul. 2016, Art. no. 023510.

[17] J.-W. Han, J. Sub Oh, and M. Meyyappan, "Vacuum nanoelectronics: Back to the future?—Gate insulated nanoscale vacuum channel transistor," *Appl. Phys. Lett.*, vol. 100, May 2012, Art. no. 213505.

[18] A. D. Bartolomeo *et al.*, "Field emission in ultrathin $PdSe_2$ back-gated transistors," *Adv. Electron. Mater.*, vol. 6, no. 7, 2020, Art. no. 2000094.

[19] M. Le-Huu *et al.*, "Investigation of the reliability of 4H–SiC MOS devices for high temperature applications," *Microelectron. Rel.*, vol. 51, no. 8, pp. 1346–1350, Aug. 2011.

[20] M. Sometani *et al.*, "Temperature-dependent analysis of conduction mechanism of leakage current in thermally grown oxide on 4H-SiC," *J. Appl. Phys.*, vol. 117, no. 2, Jan. 2015, Art. no. 024505.

[21] J. Frenkel, "On pre-breakdown phenomena in insulators and electronic semi-conductors," *Phys. Rev.*, vol. 54, no. 8, pp. 647–648, Oct. 1938.

[22] J. G. Simmons, "Poole-Frenkel effect and Schottky effect in metal-insulator-metal systems," *Phys. Rev.*, vol. 155, pp. 657–660, Mar. 1967.

[23] W. M. Jones, "Nanoscale field emission devices," Ph.D. dissertation, Dept. Elect. Eng., CALTECH, Pasadena, CA, USA, 2018.

[24] C. Davisson and L. H. Germer, "The thermionic work function of tungsten," *Phys. Rev.*, vol. 20, no. 4, pp. 300–330, Oct. 1922.

[25] M. Ghaderi, N. P. Ayerden, G. de Graaf, and R. F. Wolffenbuttel, "Minimizing stress in large-area surface micromachined perforated membranes with slits," *J. Micromech. Microeng.*, vol. 25, no. 7, Jun. 2015, Art. no. 074010.

[26] V. V. Zhirnov, C. Lizzul-Rinne, G. J. Wojak, R. C. Sanwald, and J. J. Hren, "'Standardization' of field emission measurements," *J. Vac. Sci. Technol. B, Microelectron.*, vol. 19, pp. 87–93, Jan. 2001.

[27] R. H. Fowler and L. Nordheim, "Electron emission in intense electric fields," *Proc. R. Soc. Lond. A, Math. Phys. Sci.*, vol. 119, no. 781, pp. 173–181, May 1928.

[28] S.-D. Liang, "Fowler-Nordheim theory," in *Quantum Tunneling And Field Electron Emission Theories*. Singapore: World Scientific, 2014, ch. 12, pp. 157–207.

[29] V. T. Binh and V. Semet, "Planar cold cathodes," in *Advances in Imaging and Electron Physics*, vol. 148. Amsterdam, The Netherlands: Elsevier, 2007, pp. 1–73.

[30] A. A. G. Driskill-Smith, D. G. Hasko, and H. Ahmed, "Nanoscale field emission structures for ultra-low voltage operation at atmospheric pressure," *Appl. Phys. Lett.*, vol. 71, no. 21, pp. 3159–3161, Nov. 1997.

[31] W. M. Jones, D. Lukin, and A. Scherer, "Practical nanoscale field emission devices for integrated circuits," *Appl. Phys. Lett.*, vol. 110, no. 26, Jun. 2017, Art. no. 263101.

[32] S. Dushman, "Electron emission from metals as a function of temperature," *Phys. Rev.*, vol. 21, no. 6, pp. 623–636, Jun. 1923.

[33] P. H. Cutler, J. He, J. Miller, N. M. Miskovsky, B. Weiss, and T. E. Sullivan, "Theory of electron emission in high fields from atomically sharp emitters: Validity of the Fowler-Nordheim equation," *Prog. Surf. Sci.*, vol. 42, nos. 1–4, pp. 169–185, Jan. 1993.

[34] W. P. Dyke and W. W. Dolan, "Field emission," in *Advances in Electronics and Electron Physics*, vol. 8. New York, NY, USA: Academic, Jan. 1956, pp. 89–185.

[35] C. M. Tan, J. Jia, and W. Yu, "Temperature dependence of the field emission of multiwalled carbon nanotubes," *Appl. Phys. Lett.*, vol. 86, no. 26, Jun. 2005, Art. no. 263104.

[36] J. Li, J. Chen, B. Shen, X. Yan, and Q. Xue, "Temperature dependence of the field emission from the few-layer graphene film," *Appl. Phys. Lett.*, vol. 99, Oct. 2011, Art. no. 163103.

[37] K. L. Jensen, "An analytical model of an emission-gated Twystrode using a field emitter array," *J. Appl. Phys.*, vol. 83, no. 12, pp. 7982–7992, Jun. 1998.

[38] F. Charbonnier, "Arcing and voltage breakdown in vacuum microelectronics microwave devices using field emitter arrays: Causes, possible solutions, and recent progress," *J. Vac. Sci. Technol. B, Microelectron. Nanometer Struct.*, vol. 16, no. 2, p. 880, Mar. 1998.

[39] J. Chen, J. Li, J. Yang, X. Yan, B.-K. Tay, and Q. Xue, "The hysteresis phenomenon of the field emission from the graphene film," *Appl. Phys. Lett.*, vol. 99, no. 17, Oct. 2011, Art. no. 173104.

[40] H. Yin *et al.*, "Fabrication and temperature-dependent field-emission properties of bundlelike VO_2 nanostructures," *ACS Appl. Mater. Interfaces*, vol. 3, no. 6, pp. 2057–2062, Jun. 2011.

[41] E. O. Popov, A. G. Kolosko, and S. V. Filippov, "Electrical field admissible values for the classical field emitter regime in the study of large area emitters," *AIP Adv.*, vol. 9, no. 1, Jan. 2019, Art. no. 015129.

[42] A. Di Bartolomeo *et al.*, "A WSe_2 vertical field emission transistor," *Nanoscale*, vol. 11, no. 4, pp. 1538–1548, Jan. 2019.

[43] J.-W. Han, M.-L. Seol, D.-I. Moon, G. Hunter, and M. Meyyappan, "Nanoscale vacuum channel transistors fabricated on silicon carbide wafers," *Nature Electron.*, vol. 2, no. 9, pp. 405–411, Sep. 2019.

[44] K. Subramanian, W. P. Kang, and J. L. Davidson, "Nanocrystalline diamond lateral vacuum microtriode," *Appl. Phys. Lett.*, vol. 93, no. 20, Nov. 2008, Art. no. 203511.